

# A Riemannian Take on Distance Fields and Geodesic Flows in Robotics

Journal Title  
 XX(X):1–16  
 ©The Author(s) 0000  
 Reprints and permission:  
[sagepub.co.uk/journalsPermissions.nav](http://sagepub.co.uk/journalsPermissions.nav)  
 DOI: 10.1177/ToBeAssigned  
[www.sagepub.com/](http://www.sagepub.com/)



Yiming Li<sup>1,2,\*</sup>, Jiacheng Qiu<sup>1,\*</sup> and Sylvain Calinon<sup>1,2</sup>

## Abstract

Distance functions are crucial in robotics for representing spatial relationships between the robot and the environment. It provides an implicit representation of continuous and differentiable shapes, which can seamlessly be combined with control, optimization, and learning techniques. While standard distance fields rely on the Euclidean metric, many robotic tasks inherently involve non-Euclidean structures. To this end, we generalize the use of Euclidean distance fields to more general metric spaces by solving a Riemannian eikonal equation, a first-order partial differential equation, whose solution defines a distance field and its associated gradient flow on the manifold, enabling the computation of geodesics and globally length-minimizing paths. We show that this *geodesic distance field* can also be exploited in the robot configuration space. To realize this concept, we exploit physics-informed neural networks to solve the eikonal equation for high-dimensional spaces, which provides a flexible and scalable representation without the need for discretization. Furthermore, a variant of our neural eikonal solver is introduced, which enables the gradient flow to march across both task and configuration spaces. As an example of application, we validate the proposed approach in an energy-aware motion generation task. This is achieved by considering a manifold defined by a Riemannian metric in configuration space, effectively taking the property of the robot's dynamics into account. Our approach produces minimal-energy trajectories for a 7-axis Franka robot by iteratively tracking geodesics through gradient flow backpropagation.

Project page: <https://sites.google.com/view/geodf>

## Keywords

Differential Geometry, Riemannian Manifold, Distance Field, Geodesic, Eikonal Equation, Gradient Flow, Energy-aware Motion Generation

## 1 Introduction

In robotics, measuring distances constitutes a fundamental concept for determining spatial relationships and enabling effective physical and non-physical interactions with the environment. These metrics provide a systematic means for quantifying the geometric relationships between various entities, such as points, poses, shapes or trajectories. They are widely applicable across robotic tasks, including inverse kinematics (Chiacchio et al. 1991) and motion planning (Ratliff et al. 2009). Signed distance fields (SDFs), in particular, have gained popularity for representing geometries using implicit functions, as they enable efficient distance and gradient queries which are suitable to integrate into learning (Weng et al. 2022), optimization (Li et al. 2024b) and control (Liu et al. 2022).

SDFs are conventionally employed in Euclidean spaces, representing the shortest distance from any point in the environment to the boundary of a given object or surface (Park et al. 2019). However, many robot tasks inherently operate in non-Euclidean spaces, with manifolds that can be described implicitly by a smoothly varying weighting matrix locally measuring distances. For example, distance fields can also be applied to joint configuration space, where SDFs indicate the minimum joint motion required by the robot to establish contact with a given point or object (Li et al. 2024a). In this case, the proposed extension to *geodesic distance fields* allows inertia, stiffness or manipulability

ellipsoids to be taken into account in the processing, by providing a Riemannian metric constructed with a smoothly varying symmetric positive definite (SPD) weighting matrix in the robot configuration space. Riemannian geometry provides a principled and systematic approach to generalize algorithms from Euclidean spaces to more general manifolds (Calinon 2020).

In motion planning, many approaches focus on generating optimal or feasible trajectories having a minimal length, with Euclidean distance fields often used for their differentiability and computational efficiency (Ratliff et al. 2009; Koptev et al. 2022). These trajectories are typically tracked by controllers to ensure the planned paths are precisely followed. While effective at the kinematic level, such methods neglect the robot's intrinsic dynamic properties, potentially leading to limitations in performance, stability, and robustness (Albu-Schäffer and Sachtler 2022). In contrast, differential geometry enables motion generation to incorporate these dynamic properties by identifying minimal-length geodesics on non-Euclidean manifolds. On such manifolds, the geometric properties reflect the system's inherent mechanics, and geodesics represent curved paths that minimize energy (Bullo and Lewis 2004; Biess 2013).

<sup>1</sup>Idiap Research Institute, Switzerland.

<sup>2</sup>École Polytechnique Fédérale de Lausanne (EPFL), Switzerland

\*Equal Contribution

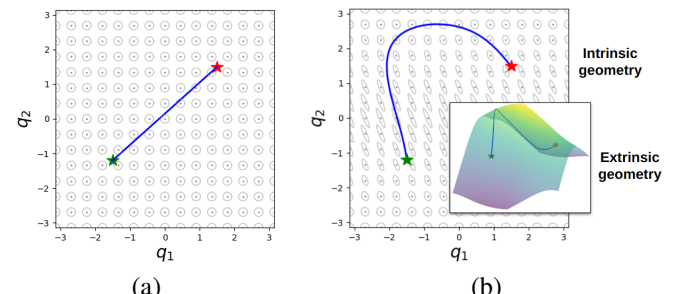
Email: name.surname@idiap.ch

Figure 1 shows minimal-distance paths in the Euclidean space and on another Riemannian manifold, where the latter provides energy-efficient paths shaped by the manifold's geometry, which can for example reflect the robot's dynamic property.

Although several methods have been proposed to compute geodesics on manifolds, these approaches often rely on local approximations and lack a comprehensive view of the entire manifold structure (Jaquier and Asfour 2022; Klein et al. 2023). These limitations can be addressed by constructing a geodesic distance field through a propagation/diffusion process, thus extending the notion of distance fields to Riemannian manifolds. The constructed *geodesic distance field* captures the manifold's global structure. It provides a continuous and differentiable representation with efficient distance and gradient queries. This advancement opens the door to extending distance-field-based learning, optimization, and control approaches to non-Euclidean manifolds, enabling more robust and dynamic-aware solutions for varied robot tasks.

This article investigates the use of *geodesic distance fields* on configuration space manifolds, focusing specifically on Riemannian manifolds defined by kinetic energy and energy conservation metrics. On such manifolds, distance fields encode minimal geodesic lengths, corresponding to the optimal energy required by the robot to perform a movement. The geodesics (minimal energy trajectories) are obtained by computing the gradient of the distance field. To construct these fields, we need to solve a Riemannian eikonal equation, a first-order partial differential equation (PDE) simulating the propagation of a wavefront on the Riemannian manifold. This approach draws inspiration from recent works using SDFs that utilize viscosity solutions to solve the eikonal equation (Gropp et al. 2020; Marić et al. 2024). By solving the eikonal equation for the distance and gradient field on anisotropic metric spaces, our approach reveals energy flow patterns on the configuration space manifold, allowing for iterative geodesic backtracking.

Traditional numerical methods for solving the eikonal equation, such as Fast Marching Method (FMM) (Sethian 1996) and its extension to the Riemannian manifold Riemannian Fast Marching (RFM) (Mirebeau 2017), rely on discretized Cartesian grids. While these methods provide deterministic solutions under given conditions, their accuracy depends on grid resolution, and they face scalability issues in high-dimensional spaces. To address these limitations, we exploit recent developments in solving eikonal equations on the Riemannian manifold using neural PDE solvers (Raissi et al. 2019; Kelshaw and Magri 2024). Unlike grid-based methods, neural solvers compute gradients through backpropagation, circumventing the curse of dimensionality and enabling the generation of continuous energy fields. Moreover, neural networks allow more flexible parameterization, which is able to encode start and goal pairs directly for the geodesic flow, whereas numerical methods typically solve the problem only for a given source point, see Figure 2. Once the model is trained, it can generalize to arbitrary state-to-goal pairs, offering rapid inference time on the order of milliseconds, which enables real-time motion planning.



**Figure 1.** Minimal distance paths as geodesics in the Euclidean space (a) and in another Riemannian metric space (b). The ellipses depict the SPD weighting matrices used to locally compute distances with this metric (isocontours of inverse matrices). A Riemannian manifold can be described intrinsically by the depicted metric. For visualization, it can also be depicted with corresponding extrinsic geometry in a higher dimensional space (see inset), but geodesic computation does not require this construction and instead only requires the metric as an intrinsic geometry representation.

We further extend our approach by introducing a variant of the *Neural Riemannian Eikonal Solver* (NES) tailored to energy-efficient inverse kinematics (NES-IK). This variant exploits a differentiable forward kinematics function as a mapping between configuration space and operational space. Here, the neural network takes a joint configuration (in the configuration space) and a target end-effector full pose (in task space) as inputs and predicts the minimal geodesic distance, indicating the energy-optimal path for the inverse kinematics solution. In other words, the neural eikonal solver allows for the propagation from the goal pose to any joint configurations while respecting the metric constraints of the configuration space manifold. Both inverse kinematics and the eikonal equation are simultaneously and implicitly learned through neural network parameterization. Geodesics are then backtracked via the derivatives with respect to the current joint configuration.

A notable advantage of this approach lies in its self-supervised nature. Both NES and NES-IK directly exploit the physical laws embedded in the eikonal equation, eliminating the need for pre-generated training data. This property, combined with its scalability, flexibility, and real-time applicability, underscores the potential of our framework for generating energy-efficient and dynamically-aware motion policies.

To demonstrate the advantages of our approach, we first conducted experiments on a planar robot to provide both quantitative and qualitative results. Subsequently, we evaluated the approach on a 7-axis Franka robot, showcasing its capability to handle high-dimensional systems and generate energy-efficient motion policies on configuration space manifolds defined by Riemannian metrics. Furthermore, we explored how to combine this motion policy with other objectives, such as constrained motion and collision avoidance, through a task-prioritization approach. This integration ensures that once the model is trained to represent energy flows for a manipulator, it can be re-used as a local motion policy in arbitrary environments.

In summary, the contributions of this work are as follows:

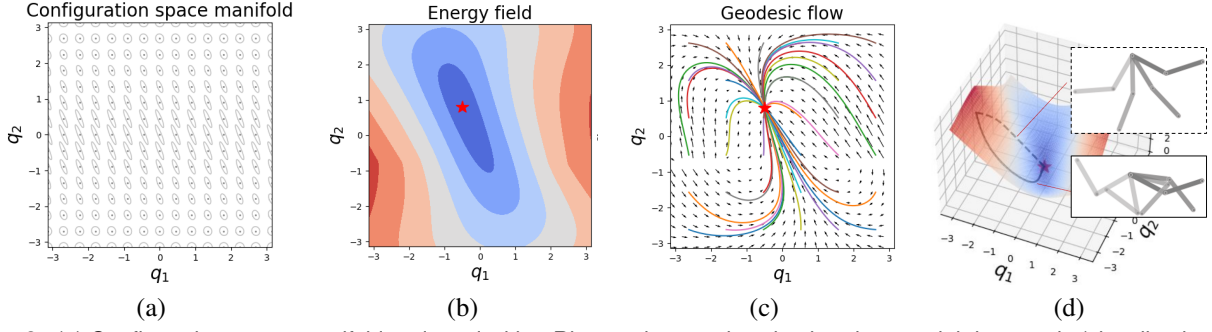


**Figure 2.** (a) Configuration space manifold endowed with a Riemannian metric using inertia as weighting matrix (visualized as isocontours of inverse matrices). The geodesics on this manifold correspond to minimal kinetic energy paths. By starting from a given point (red star), we can solve the eikonal equation on this manifold, accounting for the distance field (b) and gradient flow (c), which can then be used to backtrack geodesics in a very rapid manner (in milliseconds), see colored paths for examples of retrieved trajectories. Here, the source point is fixed for visualization. By using the proposed Neural Riemannian Eikonal Solver (NES), these points are given as inputs, meaning that geodesics from any starting point to any final point are considered altogether. (d) Geodesic path (solid line) and Euclidean path (dashed line) on this manifold with corresponding robot motions.

- We extend the principle of configuration distance fields (Li et al. 2024a) to Riemannian metric spaces, enabling broader applications in robotics beyond Euclidean distances, including energy-aware motion planning.
- To construct distance fields on high-dimensional manifolds, we propose a neural network-based parameterization of the Riemannian eikonal equation. This approach enables continuous distance field representation and geodesic flow computation, supporting efficient inference and generalizing to arbitrary point pairs after training.
- We introduce a variant of our neural eikonal solver that computes distance fields and gradient flows between task and configuration spaces, providing minimal geodesic distance solutions for inverse kinematics on a given configuration space manifold.
- We validate the effectiveness of our method through experiments with planar robots and a 7-axis Franka robot, demonstrating the generation of energy-efficient motion policies. Furthermore, we propose a task-prioritization scheme to integrate these policies with other objectives, showcasing the flexibility of our approach.

The rest of the article is structured as follows: Section 2 provides the necessary mathematical background. Section 3 reviews related work. Section 4 details our proposed method for solving the Riemannian eikonal equation to compute distance fields and geodesic flows. In Section 5, we extend this approach to map task and joint spaces for inverse kinematics problems. Finally, Section 6 presents experimental results demonstrating the effectiveness of our method, and Section 7 concludes the paper with a discussion of findings and future directions.

## 2 Background

Constructing a geodesic distance field requires solving a Riemannian eikonal equation. In this section, we introduce the mathematical background of Riemannian manifolds,

geodesics, and the eikonal equation. We also describe the Riemannian metrics on the configuration space manifolds that correspond to kinetic energy and energy conservation metrics.

### 2.1 Riemannian Metrics and Geodesics

A  $d$ -dimensional Riemannian manifold  $\mathcal{M}$  is a topological space equipped with a smooth metric tensor  $G(x)$  defined at each point  $x \in \mathcal{M}$ . The metric tensor  $G(x)$  is a symmetric positive definite matrix that defines the Riemannian metric, allowing us to calculate distances and angles on the manifold. For each point  $x \in \mathcal{M}$ , there exists a tangent space  $T_x\mathcal{M}$ , which locally linearizes the manifold.

The inner product of two velocity vectors,  $u$  and  $v$ , in the tangent space  $T_x\mathcal{M}$  at a point  $x \in \mathcal{M}$  is given by

$$\langle u, v \rangle_G = u^\top G(x)v. \quad (1)$$

Using this inner product, we define the Riemannian norm of a vector  $u$  as

$$\|u\|_G = \sqrt{\langle u, u \rangle_G}. \quad (2)$$

These definitions allow us to measure vector lengths and angles within the tangent space  $T_x\mathcal{M}$ . With this, we can define the Riemannian distance between two points,  $x_1$  and  $x_2$ , on the given manifold as

$$U(x_1, x_2) = \int_{t_0}^{t_1} \|\dot{x}(t)\|_{G(x)} dt, \quad (3)$$

where  $x(t)$  is a smooth curve connecting  $x_1$  and  $x_2$ , with  $x(t_0) = x_1$  and  $x(t_1) = x_2$ . The minimization of this expression allows us to define geodesic distances and shortest geodesic paths between two points on the manifold. Correspondingly, the curve energy is defined as

$$E(x_1, x_2) = \frac{1}{2} \int_{t_0}^{t_1} \|\dot{x}(t)\|_{G(x)}^2 dt. \quad (4)$$

Geodesics are curves that minimize this distance, which can be derived from the second-order differential equation

$$\ddot{x}_i + \Gamma_{jk}^i \dot{x}_j \dot{x}_k = 0, \quad (5)$$

where  $\Gamma_{jk}^i$  are the Christoffel symbols given by

$$\Gamma_{jk}^i = \frac{1}{2} G_{il}^{-1} \left( \frac{\partial G_{lj}}{\partial x_k} + \frac{\partial G_{lk}}{\partial x_j} - \frac{\partial G_{jk}}{\partial x_l} \right). \quad (6)$$

The Christoffel symbols describe how the coordinate systems change across the manifold. In the equation,  $G_{lj}$  represents the components of the metric tensor, while  $x_i$  are the components of the position vector  $\mathbf{x}$ . The geodesic equation essentially governs the motion of points along the shortest paths on the manifold, considering how the space curves.

## 2.2 Laplace–Beltrami operator

The Laplace–Beltrami operator is a second-order differential operator that generalizes the classical Laplace operator from Euclidean space to Riemannian manifolds. This extension is essential for analyzing functions on curved spaces, as it accounts for the geometry of the manifold. The Laplace–Beltrami operator allows us to compute the divergence of the gradient in more general spaces and is given by the expression

$$\Delta f = \frac{1}{\sqrt{|G|}} \frac{\partial}{\partial_i} \left( \sqrt{|G|} G^{ij} \frac{\partial}{\partial_j} f \right), \quad (7)$$

where  $G^{ij}$  are the components of the inverse of the metric tensor and  $|G|$  is the determinant of  $G$ .

An alternative, more compact form of the Laplace–Beltrami operator is

$$\Delta f = G^{ij} \left( \frac{\partial^2}{\partial_i \partial_j} f - \Gamma_{ij}^k \frac{\partial}{\partial_k} f \right), \quad (8)$$

where  $\Gamma_{ij}^k$  are the Christoffel symbols formulated in (6). This expression reveals that the Laplace–Beltrami operator combines the second derivatives of  $f$  with terms involving the Christoffel symbols to account for the curvature of the manifold.

## 2.3 Eikonal Equation

The eikonal equation is a nonlinear first-order partial differential equation (PDE) that models the propagation of wavefronts. Given a speed model, solving this equation provides the arrival time of the wavefront from a source point, which corresponds to the distance field and the continuous shortest path. The standard form of the eikonal equation is

$$\|\nabla U\| = c(\mathbf{x}) \quad \text{s.t.} \quad U|_{\mathbf{x}_1} = 0, \quad (9)$$

where  $U : \mathbf{x}_2 \rightarrow d(\mathbf{x}_1, \mathbf{x}_2)$  is a distance function defined over a domain of  $\mathbb{R}^n$ , and  $\mathbf{x}_1$  is the fixed source point that defines the boundary condition. Here,  $c(\mathbf{x})$  represents the speed model that influences the propagation of the wavefront. The function  $U(\mathbf{x}_2)$  with fixed source point  $\mathbf{x}_1$  is referred to as *single-point* solution. For global distance field solutions, we can encode  $U(\mathbf{x}_1, \mathbf{x}_2)$  as a function of arbitrary source-goal point pairs.

In Euclidean space, the eikonal equation describes the distance field, giving the shortest path between points. However, this equation can also be generalized to other

curved spaces such as Riemannian manifolds:

$$\|\nabla U\|_{G(\mathbf{x})} = c(\mathbf{x}) \quad \text{s.t.} \quad U|_{\mathbf{x}_1} = 0, \quad (10)$$

which describes the propagation of wavefronts on a curved surface, representing the minimal distance between the source and target points along the manifold endowed with a Riemannian metric  $G$ .

A common numerical approach for solving eikonal equations is the Fast Marching Method (FMM). Like Dijkstra's algorithm, FMM relies on the discretization of the domain and sequentially propagates information from the boundary or the solved nodes on the mesh (Sethian 1996). This method can be extended to non-Euclidean domains, allowing for the computation of geodesic distances on manifolds (Kimmel and Sethian 1998). More recent advancements leverage machine learning techniques to approximate solutions, bypassing the need for discretization and instead producing continuous, differentiable representations of distance fields in Euclidean spaces (Grubas et al. 2023) as well as on nonlinear manifolds (Kelshaw and Magri 2024).

## 2.4 Robot Dynamics on Configuration Space Manifolds

The Lagrange method is a common analytical approach for deriving the motion equation of a dynamic system. The Lagrangian function, which is used to derive the system's equations of motion, is defined as a scalar function

$$L(\mathbf{q}, \dot{\mathbf{q}}) = T(\mathbf{q}, \dot{\mathbf{q}}) - P(\mathbf{q}), \quad (11)$$

where  $T(\mathbf{q}, \dot{\mathbf{q}})$  is the kinetic energy,  $P(\mathbf{q})$  is the potential energy, and  $\mathbf{q}$  is the joint angle in the configuration space. The action functional, which describes the system's total action from time  $t_0$  to  $t_1$ , is obtained by integrating the Lagrangian:

$$S(\mathbf{q}) = \int_{t_0}^{t_1} L(\mathbf{q}(t), \dot{\mathbf{q}}(t)) dt. \quad (12)$$

Among all possible paths that satisfy the boundary conditions  $\mathbf{q}(t_1) = \mathbf{q}_1$  and  $\mathbf{q}(t_2) = \mathbf{q}_2$ , the Euler-Lagrange equation finds the path where each configuration  $\mathbf{q}$  is at the stationary point, by applying the calculus of variation:

$$\frac{d}{dt} \left( \frac{\partial L}{\partial \dot{\mathbf{q}}} \right) - \frac{\partial L}{\partial \mathbf{q}} = \mathbf{0}. \quad (13)$$

Substituting the Lagrangian  $L$  from the expression above into the Euler-Lagrange equation results in the system's equation of motion under zero external generalized forces:

$$\mathbf{M}(\mathbf{q}) \ddot{\mathbf{q}} + \mathbf{b}(\mathbf{q}, \dot{\mathbf{q}}) \dot{\mathbf{q}} + \mathbf{g}(\mathbf{q}) = \boldsymbol{\tau}, \quad (14)$$

where  $\mathbf{M}(\mathbf{q})$  is the generalized mass matrix,  $\mathbf{b}(\mathbf{q}, \dot{\mathbf{q}})$  contains the Coriolis and centrifugal terms and  $\mathbf{g}(\mathbf{q})$  is the gravity vector. We introduce two Riemannian metrics that correspond to the equations of motion:

**2.4.1 Kinetic Energy Metric** The kinetic energy of the robot in generalized coordinates is given by

$$T(\mathbf{q}, \dot{\mathbf{q}}) = \frac{1}{2} \dot{\mathbf{q}}^\top \mathbf{M}(\mathbf{q}) \dot{\mathbf{q}}, \quad (15)$$

where  $M(\mathbf{q})$  denotes the inertia matrix, which also defines the kinetic energy metric on the configuration space manifold. This metric describes the equation of motion in the absence of gravity and external forces:

$$M(\mathbf{q})\ddot{\mathbf{q}} + b(\mathbf{q}, \dot{\mathbf{q}})\dot{\mathbf{q}} = 0, \quad (16)$$

The optimal energy trajectory corresponds to the solution of the eikonal equation (10), with the Riemannian metric defined by  $M(\mathbf{q})$ , which is the minimal-length geodesic path.

**2.4.2 Jacobi Metric** The Jacobi metric describes the geometry of the configuration space under energy conservation, derived from the total energy equation

$$E = T(\mathbf{q}, \dot{\mathbf{q}}) + P(\mathbf{q}) = \frac{1}{2}\dot{\mathbf{q}}^\top M(\mathbf{q})\dot{\mathbf{q}} + P(\mathbf{q}), \quad (17)$$

where  $E$  is the conserved total energy. The Jacobi metric is a conformal transformation of the kinetic energy metric

$$M_J(\mathbf{q}) = \frac{1}{2(E - P(\mathbf{q}))} M(\mathbf{q}), \quad (18)$$

scaling the kinetic energy metric by a factor based on the difference between the total and potential energy. The resulting equation of motion is

$$M(\mathbf{q})\ddot{\mathbf{q}} + b(\mathbf{q}, \dot{\mathbf{q}})\dot{\mathbf{q}} = g(\mathbf{q}), \quad (19)$$

where the gravitational term  $g(\mathbf{q})$  drives the motion of the robot.

### 3 Related Work

#### 3.1 Distance Fields in Robotics

Distance fields are fundamental representations in robotics, due to their capacity to implicitly encode spatial information while offering continuous, differentiable representations and efficient computational properties. This versatility has led to extensive exploration of signed distance fields (SDFs) for representing scenes and objects (Millane et al. 2024; Marić et al. 2024), with demonstrated applications in collision detection (Macklin et al. 2020), grasp synthesis (Liu et al. 2021), motion generation (Ratliff et al. 2009), and manipulation planning (Yang and Jin 2024). Moreover, distance fields are increasingly utilized as latent geometric features for downstream tasks such as dynamics models learning (Driess et al. 2022), grasp pose estimation (Breyer et al. 2021; Weng et al. 2022), and motion policy generation (Fishman et al. 2023). Recent advances have introduced distance fields encoded with joint angles (Liu et al. 2022; Koptev et al. 2022; Li et al. 2023), enabling efficient distance queries between arbitrary points and the surfaces of articulated robots. Building on this foundation, our previous work (Li et al. 2024a) extended the concept of distance fields to the configuration space, wherein the representation measures the minimal joint motion required for a robot to reach specified points. The representation of articulated robots using distance fields can be interpreted as an implicit forward/inverse kinematics model, facilitating the utilization of distance and gradient information directly

in joint space. By inherently capturing joint positions and velocities, this approach opens up new possibilities for advancing applications in reactive motion planning and control (Koptev et al. 2024).

#### 3.2 Solving Eikonal Equation for Distance Fields

The eikonal equation, which models wave propagation, is widely used to compute the shortest paths from a source point and finds applications in various domains, such as seismic tomography (Lin et al. 2009), rendering (Ihrke et al. 2007), image segmentation (Alvino et al. 2007) and collision avoidance (Garrido et al. 2013). Traditional methods like the Fast Marching Method (FMM) (Sethian 1996) solve the eikonal equation using numerical computations on discretized volumetric grids. However, these approaches face scalability challenges in high-dimensional spaces. Recent advances in physics-informed neural network (PiNN) have addressed these limitations by enabling grid-free solutions through loss functions that utilize backpropagation for gradient calculation (Raissi et al. 2019). This technique has been effectively applied to solve the eikonal equation (Smith et al. 2020). In robotics, the eikonal equation plays a critical role in training or regularizing implicit signed distance fields, which are used for shape representation (Gropp et al. 2020; Xie et al. 2022). The NTField model proposes to solve neural eikonal equations for motion planning under collision avoidance constraints in high-dimensional spaces (Ni and Qureshi 2022, 2023), resulting in fast and scalable motion generation. Beyond Euclidean space, the eikonal constraint has been extended to manifolds (Ni and Qureshi 2024). The Riemannian Fast Marching method (Mirebeau 2017) adapts the eikonal equation to anisotropic metric spaces, while the heat method (Crane et al. 2013) computes geodesic distances efficiently by leveraging heat flow. Furthermore, recent work has explored solving the neural eikonal equation on manifold spaces to generate geodesics, expanding its applicability to diverse domains (Kelshaw and Magri 2024).

#### 3.3 Motion Planning on Manifolds

Recent advances in motion planning leveraged Riemannian manifolds to tackle complex challenges. Obstacles are often treated as features that reshape the geometry of the space, allowing geodesics to naturally navigate around them and achieve collision-free motion (Ratliff et al. 2015; Laux and Zell 2021). Building on this concept, Riemannian motion policies can be used in joint space using a pullback metric (Ratliff et al. 2018). This framework was later extended to Geometric Fabrics (Van Wyk et al. 2022) by incorporating principles of classical mechanics for more adaptable motion planning. Beyond static obstacle avoidance, dynamic-aware motions have been explored through kinetic energy-based Riemannian metrics (Jaquier and Asfour 2022; Klein et al. 2023), with further extensions to the Jacobi metric to account for both kinetic and potential energy, enabling energy conservation paths (Albu-Schäffer and Sachler 2022). Additionally, Riemannian metrics have been applied to human motion modeling, where

geodesics represent minimum-effort paths in configuration space (Neilson et al. 2015). These ideas have inspired methods to transfer human arm motions to robots, facilitating more natural and human-like behavior (Klein et al. 2022). Unlike these approaches that focus on local policies or optimizing for the shortest geodesics, our method emphasizes constructing a comprehensive distance field over the entire configuration space, allowing for more flexible and efficient motion planning.

## 4 Riemannian Eikonal Solver

In this section, we present the methodology for solving the Riemannian eikonal equation to compute geodesic distances and flows on the configuration space manifold. We first present the problem formulation, followed by an overview of the Riemannian Fast Marching method. Lastly, we detail our neural network parameterization for the solution of this equation.

### 4.1 Problem Formulation

We consider a configuration space manifold  $\mathcal{M}$ , whose geometry is defined by a Riemannian metric  $G(\mathbf{q})$ , where  $\mathbf{q}$  is a joint angle pose. The objective is to find the minimal geodesic distance from a source point  $\mathbf{q}_s$  to a goal point  $\mathbf{q}$ . To achieve this, we solve the Riemannian eikonal equation with constant velocity  $c(\mathbf{q}) = 1$ , namely

$$\|\nabla U(\mathbf{q})\|_{G(\mathbf{q})} = 1 \quad \text{s.t.} \quad U(\mathbf{q}_s) = 0, \quad (20)$$

where  $U(\mathbf{q})$  is the minimal geodesic length on the manifold, defined by (3). Here we use the *single-point* formulation that omits  $\mathbf{q}_s$  for brevity. It is also referred to as the travel time  $T$  from  $\mathbf{q}_s$  to  $\mathbf{q}$ . The geodesic  $\gamma(t)$  can be solved backward in time with

$$\gamma'(t) = V(\gamma(t)) \quad \text{s.t.} \quad \gamma(0) = \mathbf{q}_s, \quad \gamma(T) = \mathbf{q}, \quad (21)$$

where  $V(\mathbf{q})$  is a vector field (geodesic flow) retrieved by

$$V(\mathbf{q}) = G(\mathbf{q})\nabla U(\mathbf{q}). \quad (22)$$

Therefore, (20) can be written as

$$\begin{aligned} \|\nabla U(\mathbf{q})\|_{G(\mathbf{q})}^2 &= \nabla U(\mathbf{q})^\top G(\mathbf{q}) \nabla U(\mathbf{q}) \\ &= (G(\mathbf{q})^{-1} V(\mathbf{q}))^\top G(\mathbf{q}) (G(\mathbf{q})^{-1} V(\mathbf{q})) \\ &= V(\mathbf{q})^\top G(\mathbf{q})^{-1} V(\mathbf{q}) \\ &= \|V(\mathbf{q})\|_{G(\mathbf{q})^{-1}}^2 = 1 \end{aligned} \quad (23)$$

In this work, we consider the kinetic energy and Jacobi metric on the configuration space manifold. Minimal-length geodesics correspond to solutions of Riemannian eikonal equations defined by  $G(\mathbf{q}) = M(\mathbf{q})^{-1}$  and  $G(\mathbf{q}) = M_J(\mathbf{q})^{-1}$ .

### 4.2 Riemannian Fast Marching

Riemannian Fast Marching (RFM) is an extension of classical Fast Marching Methods (Sethian 1996) that aims to solve the eikonal equation on anisotropic and inhomogeneous manifolds to compute geodesic distances or travel times. It adapts the original algorithm to account

for the curvature and local geometry of the manifold, as described by the Riemannian metric. Like FMM, it tackles single-point solutions of eikonal equations, proceeding by discretizing the manifold into a grid and using a finite difference scheme to approximate the solution. The wavefront starts from a fixed source point  $\mathbf{q}_s$  and marches outwards. RFM updates the travel times at each wavefront point  $\mathbf{q}_e$  based on the local metric and the values at its neighboring points:

$$U(\mathbf{q}_n) = \min_{\mathbf{q}_e \in Q_e} (U(\mathbf{q}_e) + \|\mathbf{q}_n - \mathbf{q}_e\|_{G(\mathbf{q}_e)}), \quad (24)$$

where  $Q_e$  represents the set of points on the evolving wavefront, and  $\mathbf{q}_n \in Q_n = N(\mathbf{q}_e)$  is a neighboring point. The term  $\|\mathbf{q}_n - \mathbf{q}_e\|_{G(\mathbf{q}_e)}$  denotes the Riemannian distance between the two adjacent points, computed through (1) and (2).

A detailed algorithm for calculating geodesic lengths on configuration space manifolds is described in Algorithm 1. After getting  $U(\mathbf{q})$ , geodesics from arbitrary point  $\mathbf{q}$  to the source point  $\mathbf{q}_s$  are retrieved efficiently by backtracking with (21) and (22).

---

#### Algorithm 1: Riemannian Fast Marching

---

**Input:** A discretized grid map  $\mathcal{M}$   
 $G(\mathbf{q})$ : Riemannian metric  
 $\mathbf{q}_s$ : Source point  
 $c(\mathbf{q}) = 1$ : Speed model  
**Output:**  $U(\mathbf{q})$ : Geodesic length from  $\mathbf{q}_s$  to  $\mathbf{q} \in \mathcal{M}$

**Initialization:**  
set  $U(\mathbf{q}_s) = 0$   
set  $U(\mathbf{q}) = \infty$  for all  $\mathbf{q} \neq \mathbf{q}_s$ .  
set  $Q_e = \{\mathbf{q}_s\}$  Wavefront

**Propagation Step:**  
**while** there exists  $\mathbf{q} \in \mathcal{M}$  where  $U(\mathbf{q}) = \infty$  **do**  
  **for all**  $\mathbf{q}_e \in Q_e$  **do**  
    Find  $Q_n = N(\mathbf{q}_e)$   
    **for all**  $\mathbf{q}_n \in Q_n$  **do**  
      **if**  $U(\mathbf{q}_n) = \infty$  **then**  
        Update  $U(\mathbf{q}_n)$  through (24)  
       $Q_e = Q_e \cup \{\mathbf{q}_n\}$   
   $Q_e = Q_e \setminus \{\mathbf{q}_n\}$

**Termination:**  
For all points  $\mathbf{q} \in \mathcal{M}$ ,  $U(\mathbf{q}) \neq \infty$

---

Figure 2 illustrates the use of RFM for constructing distance fields (b) and gradient flows (c) on the configuration space manifold defined by the kinetic energy metric (a). (d) shows a 3D visualization of the constructed geodesics, with a comparison to the Euclidean counterpart. It is worth noting that the formulation of the eikonal equation can naturally handle collision avoidance, by assigning zero-speed velocity to points inside obstacles  $\mathcal{O}$ , namely

$$c(\mathbf{q}) = \begin{cases} 0, & \text{for } \mathbf{q} \in \mathcal{O} \\ 1, & \text{otherwise.} \end{cases} \quad (25)$$

Figure 3 shows the results of RFM for the distance field and optimal paths in the presence of obstacles. Although

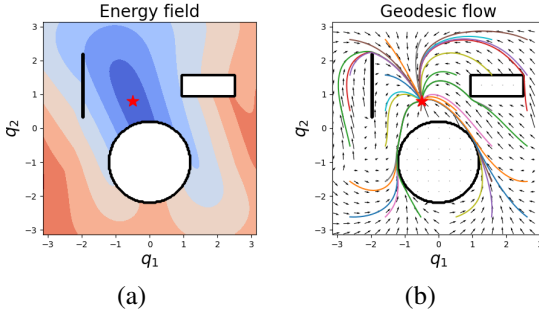


**Figure 3.** Solution of the Riemannian eikonal equation in case of obstacles (black contours) calculated using fast marching. (a) distance field. (b) Geodesic flow.

obstacles exist, the approach still finds global optimal paths without introducing additional computation complexity.

As a finite difference-based method, RFM operates a single pass on the grid, allowing efficient computation while ensuring accurate numerical results. However, the reliance on a grid or a mesh limits its scalability to high-dimensional systems such as robot manipulators. Therefore, we present a neural network parameterization to handle this problem, as discussed in the next section.

### 4.3 Neural Riemannian Eikonal Solver

The Neural Riemannian Eikonal Solver (NES) is inspired by recent developments in solving PDEs through deep neural networks. Different from classical grid-based approaches, it operates in a continuous space without the need for discretization. Gradients are calculated through network backpropagation by automatic differentiation, allowing for high-dimensional manifolds with continuously varying metrics. Instead of seeking *single-point* solutions, NES allows for global geodesic distances for arbitrary joint configuration pairs, where  $U(\mathbf{q}_s, \mathbf{q}_e)$  is a function of both source  $\mathbf{q}_s$  and goal  $\mathbf{q}_e$  points, thanks to the flexible structure provided by neural networks. Therefore, the Riemannian eikonal equation to be solved is written as

$$\|\nabla_{\mathbf{q}_e} U(\mathbf{q}_s, \mathbf{q}_e)\|_{G(\mathbf{q}_e)} = 1, \quad \text{s.t.} \quad U(\mathbf{q}_s, \mathbf{q}_s) = 0. \quad (26)$$

We introduce additional physical constraints that this equation needs to satisfy:

**Symmetry.** The geodesic distance from a source point  $\mathbf{q}_s$  to the destination point  $\mathbf{q}_e$ , and in the other direction are identical, following the symmetry property that  $U(\mathbf{q}_s, \mathbf{q}_e) = U(\mathbf{q}_e, \mathbf{q}_s)$ . It also applies to their partial derivatives:  $\nabla_{\mathbf{q}_e} U(\mathbf{q}_s, \mathbf{q}_e) = \nabla_{\mathbf{q}_e} U(\mathbf{q}_e, \mathbf{q}_s)$ . To impose this constraint, we define a symmetric function  $u_\theta^{\text{sym}}$  (Ni and Qureshi 2022)

$$u_\theta^{\text{sym}}(\mathbf{q}_s, \mathbf{q}_e) = \frac{u_\theta(\mathbf{q}_s, \mathbf{q}_e) + u_\theta(\mathbf{q}_e, \mathbf{q}_s)}{2}, \quad (27)$$

where  $u_\theta$  is the output of neural network parameterized by  $\theta$ . This equation ensures the symmetry of the network output with respect to permuted source-to-goal pairs.

**Non-negativity and non-singularity.** The geodesic distance between distinct points is strictly positive while it is zero for coincident points. It can be simply achieved by adding a non-negative activate function  $\sigma$ . However, the geodesic distance should approach zero for points close to one another, which might cause singularity issues, leading to

numerical errors in distances and gradients for points close to the source point. To overcome this problem, we follow the approach in (Kelshaw and Magri 2024; Smith et al. 2020) that factorizes the distance function as

$$U_\theta(\mathbf{q}_s, \mathbf{q}_e) = \|\mathbf{q}_e - \mathbf{q}_s\| \sigma(u_\theta^{\text{sym}}(\mathbf{q}_s, \mathbf{q}_e)), \quad (28)$$

where  $\sigma(\cdot)$  is a non-negative activation function and  $\|\mathbf{q}_e - \mathbf{q}_s\|$  is the Euclidean term between two joint configurations for non-singularity. This equation guarantees the non-negativity of geodesic distance and implicitly constrains the gradient pointing to the destination.

The parameterization involves a multi-layer perception (MLP) neural network, with a batch of concatenated joint configuration pairs  $\mathbf{q}_s$  and  $\mathbf{q}_e$  as input and outputs the predicted geodesic distance  $U_\theta(\mathbf{q}_s, \mathbf{q}_e)$ . Ground truth geodesic distances are unknown and the neural network is supervised through the physical law defined by the Riemannian eikonal equation (26). Therefore, for each source-to-goal point pair, we minimize the loss function

$$\mathbb{L}_{\text{eik}}(\mathbf{q}_s, \mathbf{q}_e) = (\|\nabla_{\mathbf{q}_e} U_\theta(\mathbf{q}_s, \mathbf{q}_e)\|_{G(\mathbf{q}_e)} - 1)^2, \quad (29)$$

to construct the geodesic distance field. The partial derivatives  $\nabla_{\mathbf{q}_e} U_\theta(\mathbf{q}_s, \mathbf{q}_e)$  are computed through automatic differentiation. In addition, to produce a smooth geodesic distance field, we add a regularization term based on the Laplace-Beltrami operator (8) which defines the divergence of the vector field:

$$\mathbb{L}_{\text{div}}(\mathbf{q}_s, \mathbf{q}_e) = G^{ij} \left( \frac{\partial^2 U(\mathbf{q}_s, \mathbf{q}_e)}{\partial q_{e,i} \partial q_{e,j}} - \Gamma_{ij}^k \frac{\partial U(\mathbf{q}_s, \mathbf{q}_e)}{\partial q_{e,k}} \right). \quad (30)$$

The Laplacian term promotes minimal curvature and local flatness, smoothing sharp or irregular regions and reducing gradient oscillations. Consequently, the resulting path is more continuous and stable when backtracking along the gradient to compute a geodesic. Therefore, the total loss function is defined as

$$\mathbb{L}_{\text{total}} = \frac{1}{N} \sum_{n=1}^N (\mathbb{L}_{\text{eik}} + \lambda \mathbb{L}_{\text{div}}), \quad (31)$$

where  $N$  is the batch size and  $\lambda$  is a hyperparameter controlling the smoothness.

## 5 Neural Riemannian Eikonal Solver for Inverse Kinematics (NES-IK)

In previous sections, we demonstrated the solution of the Riemannian eikonal equation corresponding to the minimized distance curve on the configuration space manifold and presented a neural network parameterization for solving this equation in high dimensions. Our approach reveals how geodesic flows between arbitrary joint configuration pairs on the configuration space manifold under physical constraints defined by the Riemannian metric. However, in robot manipulation, the primary focus is often on the pose of the end-effector or points of contact in task space that will interact with the environment, instead of the joint angle configurations. With the approach that we presented so far, it means that we would first have to solve the

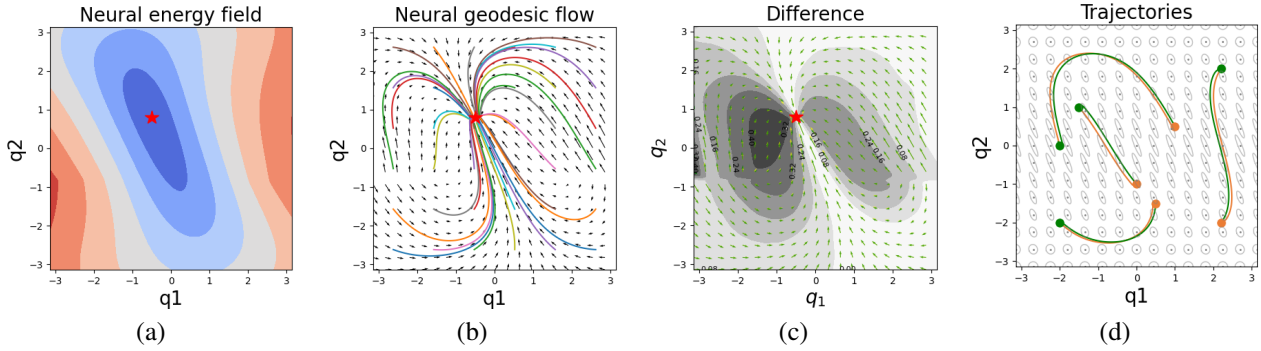


**Figure 4.** Solutions of Neural Riemannian Eikonal Solver (NES). (a) and (b) show the distance field and geodesic flow with the same parameters as Riemannian Fast Marching (RFM). (c) compares the difference with Fig. 2 (b) (c), where geodesic flows produced by NES and RFM are shown in yellow and green respectively. These three figures show that the neural network parameterization can solve the Riemannian eikonal equation, with results similar to RFM. (d) shows trajectories from source (green) to goal (orange) points and vice versa, highlighting the generalizability and symmetry of NES for arbitrary joint angle configuration pairs.

inverse kinematics problem and then backtracking minimal distance paths. However, the flexibility of our NES provides a better solution: we can directly study how the gradient flows across different spaces, particularly from the current joint angle in configuration space to a target position or orientation in task space, which satisfies robot manipulation problem specifications. The target end-effector pose  $\mathbf{x}_s$  and current joint configuration  $\mathbf{q}_e$  can be viewed as source and destination points so that the minimal-length geodesic path can be backtracked from  $\mathbf{q}_e$  to  $\mathbf{x}_s$ . Therefore, we reformulate the neural network parameterization (28) to map two spaces:

$$U_{\theta}(\mathbf{x}_s, \mathbf{q}_e) = \|f(\mathbf{q}_e) - \mathbf{x}_s\| \sigma(u_{\theta}(\mathbf{x}_s, \mathbf{q}_e)), \quad (32)$$

where  $f(\cdot)$  is the forward kinematics function. Similar to (28), the activation function  $\sigma(\cdot)$  ensures non-negativity of  $u_{\theta}$  while  $\|f(\mathbf{q}_e) - \mathbf{x}_s\|$  is a Euclidean distance term in task space. The symmetry property does not hold because  $\mathbf{x}_s$  and  $\mathbf{q}_e$  are variables from different spaces. Consequently, we use the original network output  $u_{\theta}$  instead of the symmetric version  $u_{\theta}^{sym}$ . In addition, a specific pose  $\mathbf{x}_s$  in task space might correspond to multiple joint positions solving inverse kinematics  $f^{-1}$  due to the redundancy of the manipulator. Therefore, the corresponding Riemannian eikonal equation we aim to solve is

$$\|\nabla_{\mathbf{q}_e} U(\mathbf{x}_s, \mathbf{q}_e)\|_{G(\mathbf{q}_e)} = 1 \quad \text{s.t. } U(\mathbf{x}_s, \mathbf{q}) = 0, \mathbf{q} \in f^{-1}(\mathbf{x}_s). \quad (33)$$

This equation describes the same physical constraints as (26) but with a modified boundary condition. Specifically, the distances between  $\mathbf{x}_s$  and  $\mathbf{q}$  are set to zero for all inverse kinematic solutions  $\mathbf{q} \in f^{-1}(\mathbf{x}_s)$ , which are constrained by the Euclidean term  $\|f(\mathbf{q}_e) - \mathbf{x}_s\|$ . Accordingly, the loss functions become

$$\mathbb{L}_{\text{eik}}(\mathbf{x}_s, \mathbf{q}_e) = (\|\nabla_{\mathbf{q}_e} U_{\theta}(\mathbf{x}_s, \mathbf{q}_e)\|_{G(\mathbf{q}_e)} - 1)^2, \quad (34)$$

and

$$\mathbb{L}_{\text{div}}(\mathbf{x}_s, \mathbf{q}_e) = G^{ij} \left( \frac{\partial^2 U(\mathbf{x}_s, \mathbf{q}_e)}{\partial q_{e,i} \partial q_{e,j}} - \Gamma_{ij}^k \frac{\partial U(\mathbf{x}_s, \mathbf{q}_e)}{\partial q_{e,k}} \right). \quad (35)$$

This demonstrates that we can solve the same Riemannian eikonal equation on the partial derivative  $\nabla_{\mathbf{q}_e} U$  for

inverse kinematics that minimizes geodesic distance on configuration space manifold. The only distinction lies in the forward kinematics function  $f(\cdot)$ , which is introduced as a map between two spaces and factorizes the neural network output. In other words, the neural network learns both the solution to the Riemannian eikonal equation and the inverse kinematics simultaneously. The eikonal term is explicitly learned through the loss function, while the inverse kinematics problem is implicitly learned through the factorization term  $\|f(\mathbf{q}_e) - \mathbf{x}_s\|$ . It is worth highlighting the two advantages of the proposed NES-IK:

- **End-to-end differentiability.** The network leverages gradient backpropagation through the forward kinematics function  $f(\cdot)$  to solve the inverse kinematics problem, optimizing the distance between the current end-effector position and the target point.
- **Grid-free approach.** Due to the nonlinear mapping between the task space and the configuration space, explicitly initializing a grid is infeasible without first solving the inverse kinematics problem. Consequently, traditional grid-based methods are ill-suited for this task. In contrast, the neural network addresses this challenge effectively by utilizing automatic differentiation to compute gradients.

NES-IK enables the analysis of geodesic flows across task and configuration spaces. It identifies robot motions that follow a minimal-geodesic-length curve on the configuration space manifold for inverse kinematics. In the case of redundant manipulators, when multiple solutions exist, this approach can automatically select the one with the shortest geodesic length as defined by the Riemannian metric. There are three key properties of this approach that differ from traditional optimization-based methods for inverse kinematics:

- **Metric awareness.** The approach for solving inverse kinematics typically involves the use of the Gauss-Newton algorithm, resulting in the computation of a Jacobian pseudoinverse. This method iteratively computes a least-squares solution by minimizing the

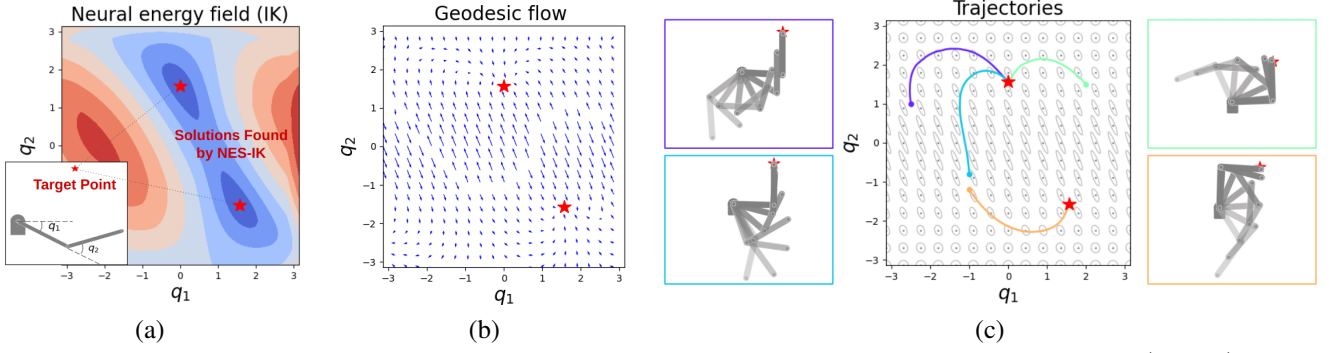


**Figure 5.** Given a kinetic energy metric, (a) and (b) show the distance field and geodesic flow for the target position (2.0, 2.0) in task space by using NES-IK. Here, we do not specify the target joint angles (red stars). These joint angle targets are instead learned implicitly by the neural network. (c) shows four robot motions in task and configuration spaces (with different colors). We can observe that the motion solution for the task in orange color differs from the other three, which is automatically computed in accordance to the distance field and geodesic flow.

Euclidean error between the desired and actual end-effector positions. Instead, our solution considers a metric space for robot motions.

- **Holistic solution.** Inverse kinematics typically focus on local solutions for joint movements. In contrast, our approach considers the optimality of the whole trajectory that corresponds to the minimum geodesic path of the configuration space manifold.
- **Real-time.** Although optimization-based approaches can also be used to find solutions for entire trajectories, they typically require iterative computations, which can be limiting for real-time applications. Instead, we leverage neural networks to approximate geodesic flows as policies. It allows us to maintain computational efficiency while ensuring that the robot’s movements are optimal solutions and can be responsive to dynamic changes.

## 6 Experiments

In this section, we demonstrate the capabilities of our NES for the energy-aware motion generation. We begin with numerical experiments, presenting quantitative and qualitative results for a 2D manipulator, and extend the analysis to high-dimensional systems using a 7-axis Franka robot. Subsequently, we validate our approach through robot experiments conducted in both simulation and real-world settings. Lastly, we explore an extension to task-prioritized, energy-efficient motion policies, illustrating the integration of our method into broader motion planning frameworks.

### 6.1 Numerical Experiments

We first conducted numerical experiments to evaluate the effectiveness of NES in energy-efficient trajectory generation. Given source-to-goal pairs, we compute the gradient of the neural network output with respect to the current joint configuration,  $\nabla_{q_e} U_\theta$ , as the joint velocity of the robot. Consequently, minimum-length geodesics are iteratively generated by following the gradient flow, corresponding to energy-optimal paths on the configuration space manifold.

**6.1.1 2D Planar Robot** We consider a planar manipulator with two links, each having a length of  $l_1 = l_2 = 2$  and masses  $m_1 = m_2 = 1$  concentrated at each articulation. The joint angle ranges from  $-\pi$  to  $\pi$  for both links. Consequently, the corresponding inertial mass matrix  $M(\mathbf{q})$  and potential energy  $P(\mathbf{q})$  can be expressed as:

$$M(\mathbf{q}) = \begin{bmatrix} (m_1 + m_2)l_1^2 + m_2l_2^2 + 2m_2l_1l_2 \cos(q_2) & m_2l_2^2 + m_2l_1l_2 \cos(q_2) \\ m_2l_2^2 + m_2l_1l_2 \cos(q_2) & m_2l_2^2 \end{bmatrix}, \quad (36)$$

$$P(\mathbf{q}) = m_1l_1 \sin(q_1) + m_2(l_1 \sin(q_1) + l_2 \sin(q_1 + q_2)), \quad (37)$$

where  $q_1$  and  $q_2$  are two joint angles. We adopt an MLP model to train NES, with concatenated source-to-goal pairs as input:  $[q_s, q_e]$  for C-space planning and  $[x_s, q_e]$  for inverse kinematics.

To demonstrate the solution of the eikonal equation corresponding to optimal energy paths on the configuration manifold, we compare trajectories generated by RFM and NES against Euclidean paths. We define two Riemannian metrics on the configuration space manifold: kinetic energy metric and Jacobi metric. In contrast to RFM which needs to reinitialize the algorithm to solve the eikonal equation when changing the source point, NES does not require recalculation and computes a batch of geodesics for random source-to-goal point pairs through the gradient computed from the neural network’s backpropagation. We report geodesic lengths  $U$  calculated from (3) for configuration pairs categorized as NEAR ( $\|q_e - q_s\| < \pi$ ), and FAR ( $\|q_e - q_s\| > 2\pi$ ) in Table 1. This table demonstrates that our neural network parameterization effectively solves the Riemannian Eikonal equation for energy-optimal paths and corresponding geodesic flows. Notably, as the distance between configuration pairs increases, the gap between Euclidean and energy-aware geodesic lengths widens, highlighting the importance of energy-aware path planning. NES outperforms RFM due to its continuous representation, without discretizing the configuration space into the grid. Qualitative results of NES for optimal kinetic energy paths are visualized in Figure 4, where (a) and (b) show the energy field and geodesic flow with the same parameters as those in the RFM setup of Figure 1, with differences highlighted in (c). Analogous trajectories are presented in (d) for arbitrary configuration pairs from source to goal and

**Table 1.** Geodesic lengths on Riemannian manifold for 2D and 7D robot motions on configuration space manifold.

Robot	Type	Method	kinetic energy metric			Jacobi metric		
			NEAR	FAR	Average	NEAR	FAR	Average
2D robot	C-Space	Euclidean Path	5.27 ± 2.98	17.40 ± 3.48	9.12 ± 5.42	4.23 ± 2.63	15.20 ± 4.36	7.38 ± 4.75
		RFM	5.05 ± 2.57	15.40 ± 3.28	7.96 ± 4.15	3.94 ± 2.10	11.26 ± 2.36	6.10 ± 3.15
		NES	4.89 ± 2.59	15.20 ± 3.23	7.82 ± 4.15	3.87 ± 2.13	11.24 ± 2.38	6.03 ± 3.18
	IK	Gauss-Newton	2.23 ± 1.49	8.19 ± 1.74	5.22 ± 2.78	1.71 ± 1.15	6.28 ± 1.42	3.98 ± 2.16
7D Franka robot	C-Space	Euclidean Path	2.01 ± 0.70	5.94 ± 1.73	4.07 ± 1.66	3.03 ± 1.66	7.48 ± 1.64	5.57 ± 2.08
		NES	1.94 ± 0.70	5.60 ± 1.46	3.84 ± 1.51	2.73 ± 1.41	6.49 ± 1.44	4.99 ± 1.79
	IK	Gauss-Newton	2.16 ± 0.41	5.32 ± 1.79	3.33 ± 1.13	3.35 ± 0.84	6.18 ± 1.02	4.41 ± 1.55
		NES-IK	1.34 ± 0.39	3.55 ± 0.71	2.75 ± 1.29	2.12 ± 0.11	4.93 ± 0.75	3.54 ± 1.23

back, emphasizing that our approach can generate symmetric paths and generalize to various configuration pairs.

In Figure 5, we illustrate the application of NES-IK in computing energy-efficient inverse kinematics solutions. The target position of the end-effector is set to  $\mathbf{x}_s = (2.0, 2.0)$ , shown in (c). This inverse kinematics problem has two possible solutions for the joint angles:  $q_1 = 0, q_2 = 1.57$  and  $q_1 = 1.57, q_2 = -1.57$ . Rather than explicitly solving the inverse kinematics problem, our approach generates the geodesic flow that iteratively guides the solution towards the minimal geodesic length, as shown in (a) and (b). Our method learns an energy-aware motion policy for inverse kinematics, with the joint angles solved iteratively and implicitly by the neural network. In (c), four robot motions, which start from various joint configurations but end at the same end-effector position, are visualized in both task space and joint space. Due to the system’s redundancy, multiple joint configurations can correspond to the same task space position, resulting in different geodesic flows starting from various joint angles. Consequently, the orange curve also represents an optimal energy solution but arrives at a different target joint configuration, distinguishing it from the other three trajectories. Quantitative comparisons are also provided in Table 1, where NEAR and FAR indicate the task space distance  $\|f(\mathbf{q}_e) - \mathbf{x}_s\| < 2.0$  and  $\|f(\mathbf{q}_e) - \mathbf{x}_s\| > 4.0$ , respectively. We chose the well-known Gauss-Newton approach as the baseline and scale the line search parameter to meet the manifold constraint. From the result, NES-IK demonstrates better motion policies for optimal energy paths on both kinetic energy and energy conservation manifold.

**6.1.2 7-axis Franka Robot** We use the 7-axis Franka robot with one degree-of-freedom redundancy to highlight the effectiveness of our approach for complex mechanical systems. The inertial mass matrix and potential energy are derived from the robot’s Unified Robot Description Format (URDF) file using the Composite Rigid Body Algorithm (Walker and Orin 1982) and we modified the implementation by (Johannessen et al. 2019) to enable batch computation in PyTorch. In addition, we observed that the determinant of the Jacobi metric  $M_J(\mathbf{q})$  calculated using (18), approaches zero and leads to substantial gradients. To address this, we scaled the determinant by 100 to stabilize the gradient field. In addition, to exploit the manifold’s local geometry structure, we adopt a geometry-aware sampling strategy, the Riemannian Manifold Metroplic Adjusted Langevin Algorithm (RM-MALA), to sample input point pairs on the configuration space manifold. A detailed description of this sampling strategy is discussed in Appendix A.1.

We employed another MLP with size [1024, 512, 256, 128, 128] to evaluate NES’s performance on the 7-axis Franka robot. During training, we randomly sampled 50’000 joint configurations  $\mathbf{q}_e$  as the edge of the wavefront points, from points generated through the RM-MALA algorithm. The model was trained for 10’000 epochs with the Adam optimizer at a learning rate of 0.001, requiring approximately four hours on a single NVIDIA RTX 3090 GPU.

In the context of inverse kinematics, NES is parameterized separately for position and orientation as

$$\begin{aligned} U_{\theta}^{\text{pos}}(\mathbf{x}_s, \mathbf{q}_e) &= \|f^{\text{pos}}(\mathbf{q}_e) - \mathbf{x}_s^{\text{pos}}\| \sigma(u_{\theta}^{\text{pos}}(\mathbf{x}_s, \mathbf{q}_e)), \\ U_{\theta}^{\text{ori}}(\mathbf{x}_s, \mathbf{q}_e) &= \arccos(f^{\text{ori}}(\mathbf{q}_e)^{\top} \mathbf{x}_s^{\text{ori}}) \sigma(u_{\theta}^{\text{ori}}(\mathbf{x}_s, \mathbf{q}_e)), \end{aligned} \quad (38)$$

where  $\|f^{\text{pos}}(\mathbf{q}_e) - \mathbf{x}_s^{\text{pos}}\|$  represents the Euclidean distance in  $\mathbb{R}^3$ , and  $\arccos(f^{\text{ori}}(\mathbf{q}_e)^{\top} \mathbf{x}_s^{\text{ori}})$  corresponds to the geodesic distance on the  $\mathcal{S}^3$  manifold. Here,  $f^{\text{ori}}(\mathbf{q}_e)$  and  $\mathbf{x}_s^{\text{ori}}$  are unit quaternions representing the orientation. The overall loss is defined as the sum of the losses induced by  $U_{\theta}^{\text{pos}}$  and the gradient flow is computed as a linear combination of gradients from  $U_{\theta}^{\text{pos}}$  and  $U_{\theta}^{\text{ori}}$ , ensuring that both position and orientation contribute to the result.

To evaluate the performance of our approach, we follow the pipeline described in Section 6.1.1, randomly sampling 100 source-to-goal pairs and comparing NES-generated geodesic lengths with baselines, on configuration manifolds endowed with both kinetic energy and Jacobi metric. Due to the high dimensionality of the robot’s configuration, the RFM baseline was unable to solve this problem. Results are presented in Table 1. For the standard Riemannian eikonal equation, NEAR and FAR denote configuration space distances, with  $\|\mathbf{q}_e - \mathbf{q}_s\| < \pi$  for NEAR and  $\|\mathbf{q}_e - \mathbf{q}_s\| > 2\pi$  for FAR. In the context of the inverse kinematics task, NEAR refers to task space distances where  $\|f^{\text{pos}}(\mathbf{q}_e) - \mathbf{x}_s^{\text{pos}}\| < 0.5$  for position and  $\arccos(f^{\text{ori}}(\mathbf{q}_e)^{\top} \mathbf{x}_s^{\text{ori}}) < \pi/2$  for orientation, while FAR denotes distances where  $\|f^{\text{pos}}(\mathbf{q}_e) - \mathbf{x}_s^{\text{pos}}\| > 1.0$  for position and  $\arccos(f^{\text{ori}}(\mathbf{q}_e)^{\top} \mathbf{x}_s^{\text{ori}}) > \pi/2$  for orientation. Results demonstrate that NES consistently generates energy-efficient paths for the 7-axis Franka robot given source-to-goal pairs in C-space, surpassing the Euclidean paths baseline. NES-IK also shows a remarkable performance in inverse kinematics compared to the Gauss-Newton method. Notably, for both Riemannian metrics, the difference between baselines and NES grows as source-to-destination distances increase, highlighting the effectiveness of NES in generating energy-efficient paths for larger robot movements, where energy efficiency is more critical.

To evaluate the computation time efficiency, we measured NES’s inference time on an NVIDIA RTX 3090 GPU and an AMD Ryzen 7 6800H CPU, with results shown in Table 2. The reported times include neural network inference, inertial mass matrix computation, and automatic differentiation for geodesic flows. For simplicity, we present one iteration computation time only for the standard Riemannian eikonal problem with source-to-goal joint configurations, which is identical to NES-IK due to their shared pipeline. The computation times are relatively low and stable across both CPU and GPU platforms, with batch sizes from 1 to  $10^3$ , supporting real-time applications. Thanks to the parallel processing capability of the GPU, efficiency is maintained even with large batch sizes. Most of the computational time is spent on inverting the Riemannian metric matrices to retrieve geodesic flows. Notably, with a batch size of 1, CPU inference time is under 0.01 seconds, enabling high-frequency updates of source-to-goal pairs, essential for reactive, real-time planning and control.

**Table 2.** Time consumption (ms) of NES.

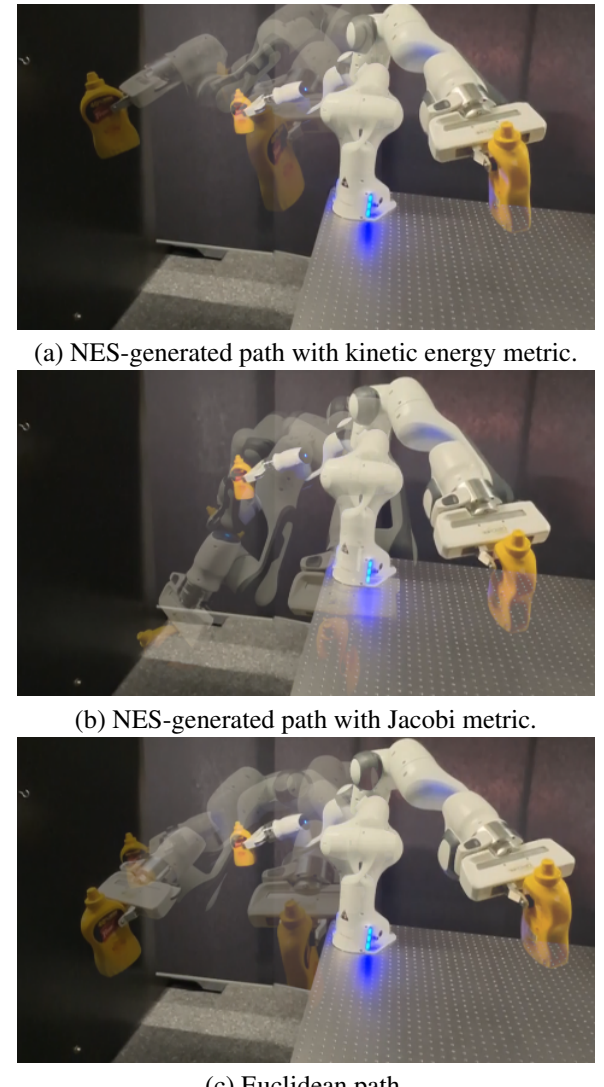
Batch Size	Kinetic energy metric		Jacobi metric	
	CPU	GPU	CPU	GPU
1	0.007	0.019	0.010	0.027
10	0.008	0.020	0.012	0.028
$10^2$	0.010	0.020	0.014	0.028
$10^3$	0.031	0.019	0.035	0.028
$10^4$	0.242	0.022	0.249	0.031
$10^5$	3.001	0.111	3.131	0.121

## 6.2 Robot Experiments

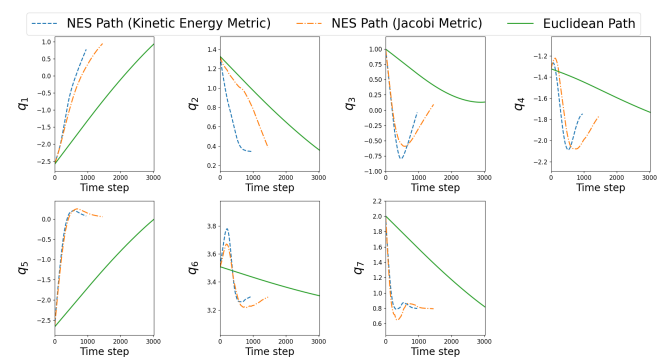
We conducted robotic experiments to demonstrate the efficacy of our approach in generating energy-aware motion policies for C-space motion planning and inverse kinematics problems, see accompanying video. As discussed in the previous section, the gradient produced by neural networks indicates the direction in which the energy flows. Therefore, we employ a joint velocity controller to track the gradient flow. To ensure stability and safety during the robot’s motion, the velocity is smoothed using the velocity at the previous time step, and the norm is scaled accordingly.

Figure 6 presents key frames of the robot trajectories generated by our NES on two configuration space manifolds, compared with the Euclidean path. For clarity, we show the joint positions for these three trajectories in Figure 7. While each trajectory shares the same start and goal points, the NES-generated paths display more natural behavior with curved trajectories in C-space, illustrating energy-efficient solutions on the configuration space manifold. The Euclidean path, represented by a straight line, is the shortest path in Euclidean space but not in Riemannian space. In addition, it requires the most time steps to reach the goal, indicating the longest geodesic length on the configuration space manifold.

Similarly, robot motions and joint positions for energy-efficient inverse kinematics are visualized in Figures 8 and 9. Although the target joint configuration is unknown, the gradient flow produced by our NES allows the robot to reach the solution iteratively, while accounting for the minimal geodesic distance path. Therefore, these three trajectories are

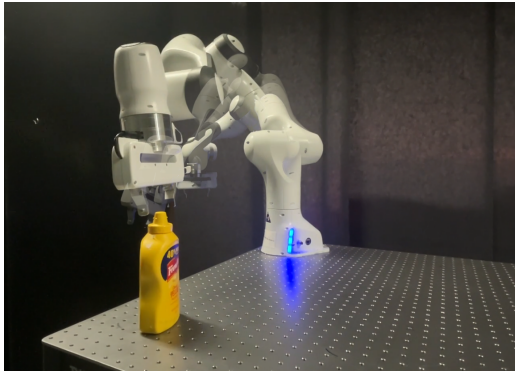


**Figure 6.** Snapshots of robot motions for C-space path planning. Initial and final frames are displayed in solid color. Intermediary frames are transparent.

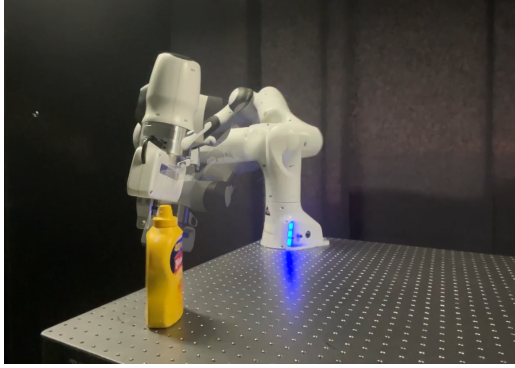


**Figure 7.** Joint positions for Euclidean and NES-generated paths.

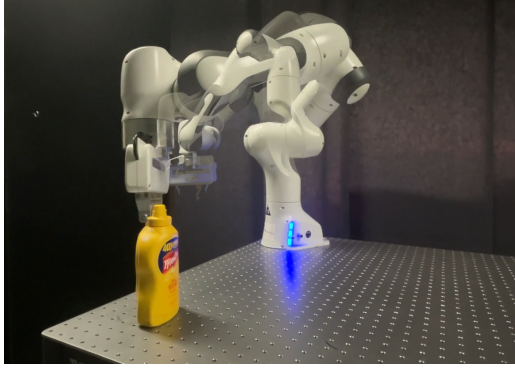
distinct from one another and lead to different final solutions due to the robot’s redundancy. Notably, for the NES-IK path with Jacobi metric (Figure 8 (b)), we observed that the robot tends to lower its body to reduce potential energy, thereby transferring it into kinetic energy. This behavior also occurs in the C-space trajectory generated by NES (Figure 6 (b)),



(a) The solution of NES-IK with kinetic energy metric.



(b) The solution of NES-IK with Jacobi metric.



(c) The solution of the Gauss-Newton method.

**Figure 8.** Snapshots of robot motions for inverse kinematics. Initial and final frames are displayed in solid color. Intermediary frames are transparent.

showing similar motion characteristics to that of humans and providing evidence of energy-efficient motion.

To further validate that geodesic paths on manifolds correspond to energy-efficient robot motions, we simulate the robot's movements to calculate energy and torque consumption. Following previous setups, we randomly initialize 100 start-to-goal pairs. For each pair, we control the robot to reach the goal with a joint velocity controller. NES and the baselines produce the input joint velocity, and we scale it to given Riemannian manifolds. At each time step, we record the current joint position and velocity to compute energy consumption. Additionally, the total torque is calculated by summing the motor torques applied to each actuator during the simulation. To ensure fair comparisons, we filter out trajectories that exceed joint limits or fail to reach the goal. Table 3 presents the results for our approach and the baselines on two manifolds. NES demonstrates superior performance in energy efficiency, showing lower

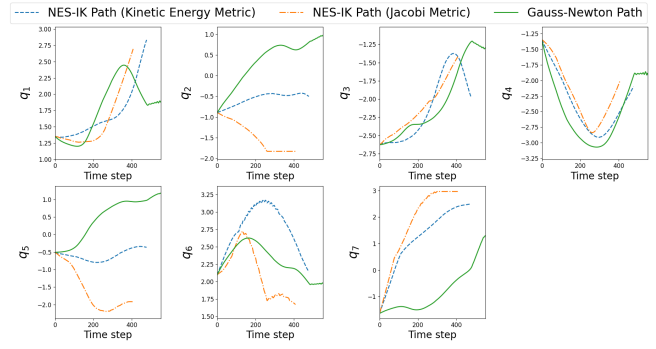
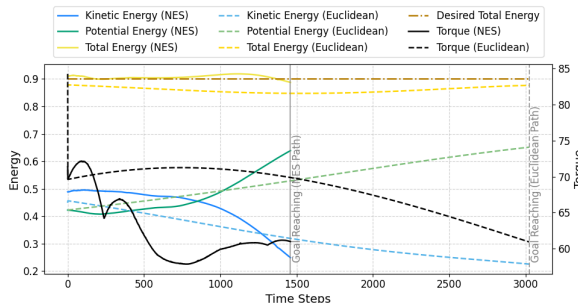


**Figure 9.** Joint positions for inverse kinematics solved by Gauss-Newton and NES-IK with kinetic energy metric and Jacobi metric.

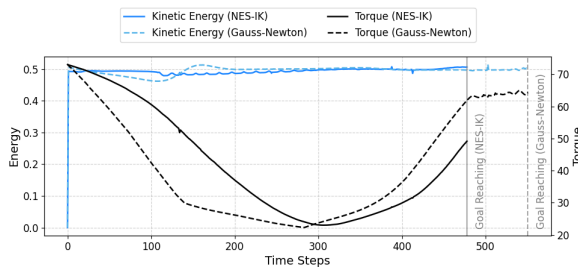
energy consumption and torque compared to the baselines on two Riemannian manifolds in both C-space motion planning and inverse kinematics tasks. The variations in energy and torque consumption during the robot's motion are illustrated in Figure 10, using the same trajectories visualized in Figure 6 and Figure 8. In Figure 10 (a), the robot moves on a manifold defined by the Jacobi metric, where the summation of kinetic and potential energy is expected to remain constant. Instead of directly moving toward the goal, the NES-generated path initially reduces the robot's potential energy, converting it into kinetic energy and resulting in a curved trajectory. This strategy requires fewer time steps to reach the goal, leading to reduced energy and torque consumption. Similarly, Figure 10 (b) illustrates kinetic energy-efficient trajectories for the inverse kinematics problem, where the kinetic energy remains constant at each time step. The solution provided by NES-IK exhibits efficient utilization of kinetic energy: although it requires higher torque at the beginning to maintain the kinetic energy, it reduces energy and torque consumption later, generating a more efficient path to reach the goal.

### 6.3 Task-prioritized Energy-efficient Motion Policy

Previous experiments have demonstrated NES's ability to generate energy-efficient motions, which is particularly beneficial for applications where energy consumption efficiency is critical. However, many real-world applications require some form of task prioritization, such as collision avoidance or adherence to environmental constraints. Although the eikonal equation offers the flexibility to modify the speed field to satisfy various constraints, re-parameterizing the neural network for each new energy field and corresponding geodesic flow is computationally demanding and impractical in dynamic environments where constraints frequently change. An alternative approach is to combine NES with other motion policies to handle multiple objectives, balancing optimality with increased flexibility and adaptability for online control. These motion policies can be integrated within the Riemannian Motion Policy (RMP) framework (Ratliff et al. 2018), leveraging the principles of operational space control (Khatib 1987). In this setup, the energy-efficiency criterion becomes a secondary task, operated in the null space of the primary task, enabling the robot to perform complex tasks while conserving energy



(a) NES and Euclidean paths with Jacobi metric.



(b) NES-IK and Gauss-Newton paths with kinetic energy metric.

**Figure 10.** Variation of energy and torque consumption among different paths and Riemannian metrics.**Table 3.** Energy and torque consumption during robot's motion.

		Kinetic Energy Metric		Jacobi Metric	
		Energy	Torque	Energy	Torque
C-Space	Euclidean Path	1.53 ± 0.62	13.4 ± 6.89	2.82 ± 0.85	12.8 ± 5.17
	NES	0.62 ± 0.18	5.14 ± 1.92	1.42 ± 0.46	6.68 ± 2.54
IK	Gauss-Newton	0.20 ± 0.09	1.56 ± 0.62	0.51 ± 0.23	2.12 ± 1.08
	NES-IK	0.15 ± 0.07	1.26 ± 0.56	0.37 ± 0.11	1.75 ± 0.88

costs. Given a function  $f(\mathbf{q})$  that constrains the joint position  $\mathbf{q}$ , the joint velocity must satisfy the constraint  $\mathbf{J}_f(\mathbf{q})\dot{\mathbf{q}} = 0$  to maintain the robot's movement within this manifold. Here,  $\mathbf{J}_f(\mathbf{q}) = \frac{\partial f}{\partial \mathbf{q}}$  is the Jacobian of the constraint function. By projecting the energy-aware policy  $\dot{\mathbf{q}}_{\text{energy}}$  generated by NES into the null space of  $\mathbf{J}_f$ , we ensure that energy-efficient motions occur only within the degrees of freedom available after fulfilling the primary task requirements, namely

$$\dot{\mathbf{q}} = (\mathbf{I} - \mathbf{J}_f^\dagger \mathbf{J}_f) \dot{\mathbf{q}}_{\text{energy}}, \quad (39)$$

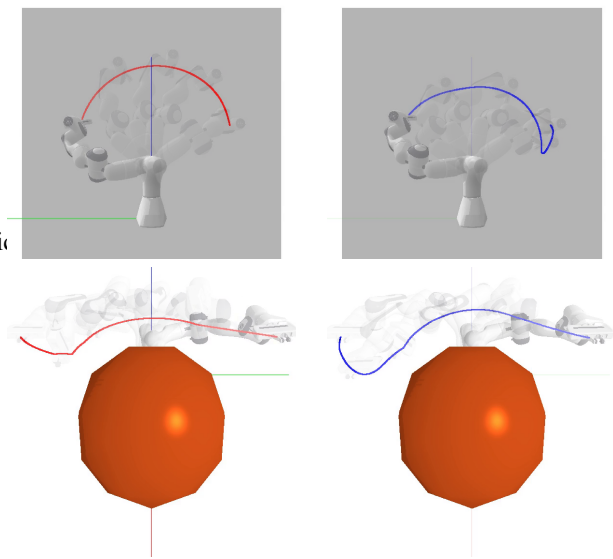
where  $\mathbf{J}_f^\dagger$  is the pseudoinverse of the Jacobian matrix.

We integrate two typical motion strategies with our energy-efficient motion policy: constrained motion and obstacle avoidance. The former task usually involves task-space constraints, such as maintaining a specific end-effector position and orientation, while obstacle avoidance requires planning a collision-free trajectory to ensure safety. The experimental setups are detailed below:

**6.3.1 Constrained motion** In this setup, the robot's end-effector is restricted to moving within a specified plane, maintaining an orthogonal orientation. The plane is parallel to the horizontal plane at  $x = 0.3$ , with the vertical axis of the end-effector aligned consistently throughout the motion. To achieve energy-efficient movement, our NES policy is designed to operate within the nullspace of the primary task. The Jacobian of the constraint function occupies a subspace within the full Jacobian matrix of the robot, allowing NES

to optimize energy usage without disrupting the primary task requirements.

**6.3.2 Obstacle avoidance** The objective of this task is to maintain energy-efficient motion while preventing collisions with surrounding obstacles. Building on prior work (Li et al. 2024b), we utilize a distance function and its gradient to monitor proximity to obstacles. When an obstacle remains at a safe distance, the robot follows the NES-generated energy-efficient policy. However, if an obstacle enters a predefined safety zone near the obstacle, the collision avoidance strategy constrains NES within the nullspace, ensuring obstacle avoidance without impacting the primary task.

**Figure 11.** Trajectories generated by task-prioritized energy-efficient motion policy and baseline. Top: Constrained motion in which the end-effector is perpendicular to a plane. Bottom: Obstacle avoidance. Red and blue curves depict the Euclidean and energy-efficient paths operating in the nullspace of each principal task.

To evaluate the performance of task-prioritized energy-efficient motion policy, we first sample 100 joint configuration pairs far from each other (with angular distance  $\|\mathbf{q}_e - \mathbf{q}_s\| > 2\pi$ ) that satisfy these two constraints then run the NES algorithm to compute energy-aware policies and project them into the nullspace of the principal tasks. Table 4 presents the experimental results on average geodesic lengths. It is clear that the introduction of constraints will increase geodesic lengths on the configuration space manifold as the space of feasible solutions is restricted. Nevertheless, the energy-optimal motion policy generated by NES remains effective in minimizing energy consumption compared to Euclidean paths. Figure 11 compares trajectories of task-prioritized motions with/without our energy-aware motion policy, demonstrating the effectiveness and flexibility of NES in combination with other motion policies for real-time, adaptive, and energy-efficient robot control. Additionally, except for the formulation of nullspace control, the geodesic flow of NES can also be viewed as non-linear dynamical systems (Khansari-Zadeh and Billard 2011) and can be easily integrated with either control frameworks such as model predictive control (MPC) (Koptev et al. 2024)

**Table 4.** Geodesic lengths for task-prioritized energy-aware motion policies on Riemannian manifolds.

Type	Jacobi Metric		Energy Conservation Metric	
	Euclidean	NES	Euclidean	NES
No Constraint	4.95±1.00	4.62±0.95	6.79±1.43	6.50±1.44
Obstacle	5.43±1.41	4.95±1.32	7.28±1.56	6.66±1.57
Constrained Motion	5.30±1.51	5.05±1.61	7.47±1.56	6.95±1.58

or learning paradigms (Florence et al. 2022) for energy conservation purpose.

## 7 Discussion and Conclusion

In this article, we generalized the use of the *geodesic distance field* in the configuration space manifold by employing intrinsic Riemannian metrics. This is accomplished by solving the eikonal equation on these manifolds, which enables the computation of geodesic distance fields and gradient flows. To address the challenges of high-dimensional configuration spaces for robot manipulators, we propose a neural network-based parameterization. This representation facilitates efficient computation of distances and geodesics, enabling globally length-minimizing paths. We extend the Neural Riemannian Eikonal Solver (NES) to compute geodesic flows across both task and configuration spaces, resulting in length-minimizing inverse kinematics solutions on the configuration space manifold. Our approach is validated in an energy-aware motion planning task, where the robot’s dynamic properties are expressed as Riemannian metrics. The proposed method demonstrates its efficiency and ability to generate energy-efficient paths for a 7-axis Franka robot. Furthermore, we discuss the integration of our geodesic flow computations with other motion policies in a task-prioritized framework.

Our approach computes distance fields directly using intrinsic geometry, with a Riemannian metric, eliminating the need for extrinsic geometry construction. The gradient flow, derived from the distance field, enables efficient propagation along minimal-distance paths by iteratively backtracking geodesics. Unlike traditional optimization-based methods, our approach directly computes optimal geodesic solutions between arbitrary source and goal point pairs. Moreover, the resulting gradient flow can function as a real-time policy, offering greater flexibility and scalability. This structure allows seamless integration with other planning, control, and optimization techniques by leveraging the distance and gradient information. Additionally, the neural network encoding allows the implicit geodesic distance to serve as a latent feature that can be integrated into various learning frameworks.

The geodesic distance field is derived from the Riemannian eikonal equation, which encapsulates physical laws governing the system. Therefore, our network is trained to satisfy these physical constraints in a self-supervised manner, without the need for generating training data. In our energy-aware motion generation application, this equation models the robot’s dynamic properties. However, it can also be adapted to represent other attributes such as stiffness or manipulability ellipsoids. By defining these properties geometrically within the configuration space manifold, the approach provides a deeper understanding of the robot’s behavior and performance. Furthermore, this geometric

representation can support robot co-design by informing adjustments to improve functionality and optimize system performance.

A key limitation of our approach lies in training the neural Riemannian eikonal solver. Once a model is trained, it can be reused multiple times, enabling efficient, real-time applications. However, the absence of prior data, coupled with the strongly anisotropic nature of the Riemannian metric, presents significant challenges. Indeed, although our formulation theoretically allows for global optimal solutions, its practical performance can sometimes unexpectedly fall short. In future work, we aim to optimize the training process for improved robustness and accuracy. In addition, we plan to apply our approach to broader metric spaces beyond Riemannian manifolds. The eikonal equation can also be extended to other differential equations for wider robot applications, such as the general equation of motion for robot dynamics (Lutter et al. 2018), value functions for dynamical programming, and reinforcement learning.

## References

- Albu-Schäffer A and Sachtler A (2022) What can algebraic topology and differential geometry teach us about intrinsic dynamics and global behavior of robots? In: *The International Symposium of Robotics Research*. Springer, pp. 468–484.
- Alvino C, Unal G, Slabaugh G, Peny B and Fang T (2007) Efficient segmentation based on eikonal and diffusion equations. *International Journal of Computer Mathematics* 84(9): 1309–1324.
- Biess A (2013) Shaping of arm configuration space by prescription of non-Euclidean metrics with applications to human motor control. *Phys. Rev. E* 87: 012729.
- Breyer M, Chung JJ, Ott L, Siegwart R and Nieto J (2021) Volumetric grasping network: Real-time 6 dof grasp detection in clutter. In: *Proc. Conference on Robot Learning (CoRL)*. PMLR, pp. 1602–1611.
- Bullo F and Lewis AD (2004) *Geometric Control of Mechanical Systems: Modeling, Analysis, and Design for Simple Mechanical Control Systems*, volume 49. Springer Science & Business Media.
- Calinon S (2020) Gaussians on riemannian manifolds: Applications for robot learning and adaptive control. *IEEE Robotics & Automation Magazine* 27(2): 33–45.
- Chiacchio P, Chiaverini S, Sciaffico L and Siciliano B (1991) Closed-loop inverse kinematics schemes for constrained redundant manipulators with task space augmentation and task priority strategy. *The International Journal of Robotics Research* 10(4): 410–425.
- Crane K, Weischedel C and Wardetzky M (2013) Geodesics in heat: A new approach to computing distance based on heat flow. *ACM Transactions on Graphics (TOG)* 32(5): 1–11.
- Driess D, Ha JS, Toussaint M and Tedrake R (2022) Learning models as functionals of signed-distance fields for manipulation planning. In: *Proc. Conference on Robot Learning (CoRL)*. PMLR, pp. 245–255.
- Fishman A, Murali A, Eppner C, Peele B, Boots B and Fox D (2023) Motion policy networks. In: *Conference on Robot Learning*. PMLR, pp. 967–977.

- Florence P, Lynch C, Zeng A, Ramirez OA, Wahid A, Downs L, Wong A, Lee J, Mordatch I and Tompson J (2022) Implicit behavioral cloning. In: *Conference on Robot Learning*. PMLR, pp. 158–168.
- Garrido S, Malfaz M and Blanco D (2013) Application of the fast marching method for outdoor motion planning in robotics. *Robotics and Autonomous Systems* 61(2): 106–114.
- Girolami M and Calderhead B (2011) Riemann manifold langevin and hamiltonian monte carlo methods. *Journal of the Royal Statistical Society Series B: Statistical Methodology* 73(2): 123–214.
- Gropp A, Yariv L, Haim N, Atzmon M and Lipman Y (2020) Implicit geometric regularization for learning shapes. In: *Proceedings of Machine Learning and Systems 2020*. pp. 3569–3579.
- Grubas S, Duchkov A and Loginov G (2023) Neural eikonal solver: Improving accuracy of physics-informed neural networks for solving eikonal equation in case of caustics. *Journal of Computational Physics* 474: 111789.
- Ihrke I, Ziegler G, Tevs A, Theobalt C, Magnor M and Seidel HP (2007) Eikonal rendering: Efficient light transport in refractive objects. *ACM Transactions on Graphics (TOG)* 26(3): 59–es.
- Jaquier N and Asfour T (2022) Riemannian geometry as a unifying theory for robot motion learning and control. In: *The International Symposium of Robotics Research*. Springer, pp. 395–403.
- Johannessen LMG, Arbo MH and Gravdahl JT (2019) Robot dynamics with urdf & casadi. In: *2019 7th International Conference on Control, Mechatronics and Automation (ICCMA)*. IEEE.
- Kelshaw D and Magri L (2024) Computing distances and means on manifolds with a metric-constrained eikonal approach. *arXiv preprint arXiv:2404.08754*.
- Khansari-Zadeh SM and Billard A (2011) Learning stable nonlinear dynamical systems with gaussian mixture models. *IEEE Transactions on Robotics* 27(5): 943–957.
- Khatib O (1987) A unified approach for motion and force control of robot manipulators: The operational space formulation. *IEEE Journal on Robotics and Automation* 3(1): 43–53.
- Kimmel R and Sethian JA (1998) Computing geodesic paths on manifolds. *Proceedings of the national academy of Sciences* 95(15): 8431–8435.
- Klein H, Jaquier N, Meixner A and Asfour T (2022) A Riemannian take on human motion analysis and retargeting. In: *2022 IEEE/RSJ International Conference on Intelligent Robots and Systems (IROS)*. IEEE, pp. 5210–5217.
- Klein H, Jaquier N, Meixner A and Asfour T (2023) On the design of region-avoiding metrics for collision-safe motion generation on riemannian manifolds. In: *2023 IEEE/RSJ International Conference on Intelligent Robots and Systems (IROS)*. IEEE, pp. 2346–2353.
- Koptev M, Figueroa N and Billard A (2022) Neural joint space implicit signed distance functions for reactive robot manipulator control. *IEEE Robotics and Automation Letters* 8(2): 480–487.
- Koptev M, Figueroa N and Billard A (2024) Reactive collision-free motion generation in joint space via dynamical systems and sampling-based mpc. *The International Journal of Robotics Research* : 02783649241246557.
- Laux M and Zell A (2021) Robot arm motion planning based on geodesics. In: *2021 IEEE International Conference on Robotics and Automation (ICRA)*. IEEE, pp. 7585–7591.
- Li Y, Chi X, Razmjoo A and Calinon S (2024a) Configuration space distance fields for manipulation planning. In: *Proc. Robotics: Science and Systems (RSS)*.
- Li Y, Zhang Y, Razmjoo A and Calinon S (2023) Learning robot geometry as distance fields: Applications to whole-body manipulation. *arXiv preprint arXiv:2307.00533*.
- Li Y, Zhang Y, Razmjoo A and Calinon S (2024b) Representing robot geometry as distance fields: Applications to whole-body manipulation. In: *Proc. IEEE Intl Conf. on Robotics and Automation (ICRA)*. pp. 15351–15357.
- Lin FC, Ritzwoller MH and Snieder R (2009) Eikonal tomography: surface wave tomography by phase front tracking across a regional broad-band seismic array. *Geophysical Journal International* 177(3): 1091–1110.
- Liu P, Zhang K, Tateo D, Jauhri S, Peters J and Chalvatzaki G (2022) Regularized deep signed distance fields for reactive motion generation. In: *Proc. IEEE/RSJ Intl Conf. on Intelligent Robots and Systems (IROS)*. IEEE, pp. 6673–6680.
- Liu T, Liu Z, Jiao Z, Zhu Y and Zhu SC (2021) Synthesizing diverse and physically stable grasps with arbitrary hand structures using differentiable force closure estimator. *IEEE Robotics and Automation Letters* 7(1): 470–477.
- Lutter M, Ritter C and Peters J (2018) Deep lagrangian networks: Using physics as model prior for deep learning. In: *International Conference on Learning Representations*.
- Macklin M, Erleben K, Müller M, Chentanez N, Jeschke S and Corse Z (2020) Local optimization for robust signed distance field collision. *Proceedings of the ACM on Computer Graphics and Interactive Techniques* 3(1): 1–17.
- Marić A, Li Y and Calinon S (2024) Online learning of continuous signed distance fields using piecewise polynomials. *IEEE Robotics and Automation Letters (RA-L)* 9(6): 6020–6026. DOI:10.1109/LRA.2024.3397085.
- Millane A, Oleynikova H, Wirbel E, Steiner R, Ramasamy V, Tingdahl D and Siegwart R (2024) nvblox: Gpu-accelerated incremental signed distance field mapping.
- Mirebeau JM (2017) Anisotropic fast-marching on cartesian grids using voronoi's first reduction of quadratic forms. *HAL (Preprint)*, April 63.
- Neilson PD, Neilson MD and Bye RT (2015) A Riemannian geometry theory of human movement: The geodesic synergy hypothesis. *Human movement science* 44: 42–72.
- Ni R and Qureshi AH (2022) Ntfields: Neural time fields for physics-informed robot motion planning. In: *The Eleventh International Conference on Learning Representations*.
- Ni R and Qureshi AH (2023) Progressive learning for physics-informed neural motion planning. *arXiv preprint arXiv:2306.00616*.
- Ni R and Qureshi AH (2024) Physics-informed neural motion planning on constraint manifolds. *arXiv preprint arXiv:2403.05765*.
- Park JJ, Florence P, Straub J, Newcombe R and Lovegrove S (2019) Deepsdf: Learning continuous signed distance functions for shape representation. In: *Proc. IEEE Conf. on Computer Vision and Pattern Recognition (CVPR)*. pp. 165–174.

- Raissi M, Perdikaris P and Karniadakis GE (2019) Physics-informed neural networks: A deep learning framework for solving forward and inverse problems involving nonlinear partial differential equations. *Journal of Computational physics* 378: 686–707.
- Ratliff N, Toussaint M and Schaal S (2015) Understanding the geometry of workspace obstacles in motion optimization. In: *2015 IEEE International Conference on Robotics and Automation (ICRA)*. IEEE, pp. 4202–4209.
- Ratliff N, Zucker M, Bagnell JA and Srinivasa S (2009) Chomp: Gradient optimization techniques for efficient motion planning. In: *Proc. IEEE Intl Conf. on Robotics and Automation (ICRA)*. IEEE, pp. 489–494.
- Ratliff ND, Issac J, Kappler D, Birchfield S and Fox D (2018) Riemannian motion policies. *arXiv preprint arXiv:1801.02854*.
- Sethian JA (1996) A fast marching level set method for monotonically advancing fronts. *proceedings of the National Academy of Sciences* 93(4): 1591–1595.
- Smith JD, Azizzadenesheli K and Ross ZE (2020) Eikonet: Solving the eikonal equation with deep neural networks. *IEEE Transactions on Geoscience and Remote Sensing* 59(12): 10685–10696.
- Van Wyk K, Xie M, Li A, Rana MA, Babich B, Peele B, Wan Q, Akinola I, Sundaralingam B, Fox D, Boots B and Ratliff ND (2022) Geometric fabrics: Generalizing classical mechanics to capture the physics of behavior. *IEEE Robotics and Automation Letters* 7(2): 3202–3209.
- Walker MW and Orin DE (1982) Efficient dynamic computer simulation of robotic mechanisms .
- Weng T, Held D, Meier F and Mukadam M (2022) Neural grasp distance fields for robot manipulation. *arXiv preprint arXiv:2211.02647*.
- Xie Y, Takikawa T, Saito S, Litany O, Yan S, Khan N, Tombari F, Tompkin J, Sitzmann V and Sridhar S (2022) Neural fields in visual computing and beyond. In: *Computer Graphics Forum*, volume 41. Wiley Online Library, pp. 641–676.
- Yang W and Jin W (2024) Contact sdf: Signed distance functions as multi-contact models for dexterous manipulation. *arXiv preprint arXiv:2408.09612* .

## A Appendix

### A.1 Geometry-Aware Sampling

We present the Riemannian Manifold Metropolis-Adjusted Langevin Algorithm (RM-MALA) for geometry-aware sampling on the Riemannian manifold. A detailed algorithm is shown in Algorithm 2.

**A.1.1 Target Probability Density Function (PDF)** In each tangent space, an infinitesimal space is induced by the Riemannian metric  $d\mathcal{M}(\mathbf{q}) = \sqrt{|\mathbf{G}(\mathbf{q})|}d\mathbf{q}$ , bridging the target probability density function (PDF)  $\rho(\mathbf{q})$  with respect to the Lesbergue measurement  $d\mathbf{q}$ , to the PDF  $p(\mathbf{q})$  with respect to  $d\mathcal{M}(\mathbf{q})$  by

$$\rho(\mathbf{q}) = p(\mathbf{q})\sqrt{|\mathbf{G}(\mathbf{q})|}. \quad (40)$$

**A.1.2 Sampling on the Riemannian manifold** The objective is to sample variables on the Riemannian manifold from the PDF  $\rho(\mathbf{q})$ , while taking into account the local geometric

structure. Given the Riemannian metric tensor, we adopt the Metropolis-adjusted Langevin Monte Carlo algorithm on the Riemannian Manifold (Girolami and Calderhead 2011). The algorithm describes the Langevin diffusion process on the Riemannian manifold in a stochastic differential equation (SDE)

$$d\mathbf{q}(t) = \frac{1}{2}\tilde{\nabla}_{\mathbf{q}}\mathcal{L}(\mathbf{q}(t)) + d\tilde{\mathbf{b}}(t), \quad (41)$$

with  $\tilde{\nabla}_{\mathbf{q}}\mathcal{L}(\mathbf{q}(t))$  representing the natural gradient equipped by the Riemannian metric tensor  $\tilde{\nabla}_{\mathbf{q}}\mathcal{L}(\mathbf{q}) = \mathbf{G}^{-1}(\mathbf{q})\nabla_{\mathbf{q}}\mathcal{L}(\mathbf{q})$ , where

$$\mathcal{L}(\mathbf{q}) = \log \rho(\mathbf{q}). \quad (42)$$

The equation of the Brownian motion  $d\tilde{\mathbf{b}}(t)$  is given by

$$\begin{aligned} d\tilde{\mathbf{b}}_i(t) &= \frac{1}{\sqrt{|\mathbf{G}(\mathbf{q}(t))|}} \sum_{j=1}^D \frac{\partial}{\partial \mathbf{q}_j} \left( (\mathbf{G}^{-1}(\mathbf{q}(t)))_{ij} \sqrt{|\mathbf{G}(\mathbf{q}(t))|} \right) dt \\ &\quad + \left( \sqrt{\mathbf{G}^{-1}(\mathbf{q}(t))} \mathbf{b}(t) \right)_i, \end{aligned} \quad (43)$$

where  $\mathbf{b}(t)$  is the normal Brownian motion. Assuming  $p(\mathbf{q})$  is a constant, the natural gradient is expressed using (40):

$$\tilde{\nabla}_{\mathbf{q}}\mathcal{L}(\mathbf{q}) = \mathbf{G}^{-1}(\mathbf{q})\nabla_{\mathbf{q}}\sqrt{|\mathbf{G}(\mathbf{q})|}. \quad (44)$$

In (41),  $d\tilde{\mathbf{b}}(t)$  defines the Brownian motion on the Riemannian manifold. After applying the first-order Euler integration with the fixed step size  $\epsilon$  to the SDE (41), we have

$$\mathbf{q}(t+1) = \mu(\mathbf{q}(t), \epsilon) + \left( \epsilon \sqrt{\mathbf{G}^{-1}(\mathbf{q}(t))} \mathbf{z}(t) \right), \quad (45)$$

where  $\mu(\mathbf{q}(t), \epsilon)$  is the mean of the Gaussian distribution associated with the sampled variable

$$\begin{aligned} \mu(\mathbf{q}(t), \epsilon) &= \mathbf{q}(t) + \frac{\epsilon^2}{2} \left( \mathbf{G}^{-1}(\mathbf{q}(t)) \nabla_{\mathbf{q}}\mathcal{L}(\mathbf{q}(t)) \right)_i \\ &\quad - \epsilon^2 \sum_{j=1}^D \left( \left( \mathbf{G}^{-1}(\mathbf{q}(t)) \right) \frac{\partial \mathbf{G}(\mathbf{q}(t))}{\partial \mathbf{q}_j} \mathbf{G}^{-1}(\mathbf{q}(t)) \right)_{ij} \\ &\quad + \frac{\epsilon^2}{2} \sum_{j=1}^D \left( \mathbf{G}^{-1}(\mathbf{q}(t)) \right)_{ij} \text{Tr} \left( \left( \mathbf{G}^{-1}(\mathbf{q}(t)) \right) \frac{\partial \mathbf{G}(\mathbf{q}(t))}{\partial \mathbf{q}_j} \right) \end{aligned} \quad (46)$$

and  $\mathbf{z}$  is a random variable sampled from the standard normal distribution  $\mathbf{z} \sim \mathcal{N}(\mathbf{z}|\mathbf{0}, \mathbf{I})$ . Finally, the probability of the sampled variable follows the Gaussian distribution

$$p(\mathbf{q}(t+1)|\mathbf{q}(t)) = \mathcal{N}(\mathbf{q}(t+1)|\mu(\mathbf{q}(t), \epsilon), \epsilon^2 \mathbf{G}^{-1}(\mathbf{q}(t))). \quad (47)$$

The acceptance of the sampled variable is finally calculated with

$$\alpha = \mathcal{L}(\mathbf{q}(t+1)) + \log p(\mathbf{q}(t)|\mathbf{q}(t+1)) - \mathcal{L}(\mathbf{q}(t)) - \log p(\mathbf{q}(t+1)|\mathbf{q}(t)). \quad (48)$$

---

**Algorithm 2:** RM-MALA

---

**Input:**  $G(\mathbf{q})$ : Riemannian metric function $\mathcal{L}(\mathbf{q})$ : Proposed likelihood function $n_{\text{burn}}$ : Burn-in steps $n_{\text{sample}}$ : Sample steps $\epsilon$ : Step size**Output:**  $Q$ : A set of sampled points  $\mathbf{q}$ **Initialization:**set Random points  $\mathbf{q} \in [-\pi, \pi)$ **Sampling Step:****for**  $i$  from 1 to  $n_{\text{burn}} + n_{\text{sample}}$  **do**    Sample new point  $\mathbf{q}_{\text{new}}$  through (45)    **if**  $\mathbf{q}_{\text{new}} \notin [-\pi, \pi)$  **then**         $\mathbf{q}_{\text{new}} = \text{arctan2}(\sin(\mathbf{q}_{\text{new}}), \cos(\mathbf{q}_{\text{new}}))$     Calculate the proposed log-likelihood  $\log \mathcal{L}(\mathbf{q})$     and  $\log \mathcal{L}(\mathbf{q}_{\text{new}})$  through (42)    Calculate the transition likelihood  $p(\mathbf{q}_{\text{new}}|\mathbf{q})$  and     $p(\mathbf{q}|\mathbf{q}_{\text{new}})$  through (47)    Calculate the acceptance ratio  $\alpha$  through (48)    Draw a random number  $t \in [0, 1)$     **if**  $e^\alpha \geq t$  **then**         $\mathbf{q} = \mathbf{q}_{\text{new}}$         **if**  $i \geq n_{\text{burn}}$  **then**            Add  $\mathbf{q}_{\text{new}}$  into set  $Q$     **else**         $\mathbf{q}_{\text{new}}$  is not accepted